



HAL
open science

Doped Graphene To Mimic the Bacterial NADH Oxidase for One-Step NAD + Supplementation in Mammals

Xi Liu, Jingkun Li, Andrea Zitolo, Meng Gao, Jun Jiang, Xiangtian Geng, Qianqian Xie, Di Wu, Huizhen Zheng, Xiaoming Cai, et al.

► **To cite this version:**

Xi Liu, Jingkun Li, Andrea Zitolo, Meng Gao, Jun Jiang, et al.. Doped Graphene To Mimic the Bacterial NADH Oxidase for One-Step NAD + Supplementation in Mammals. *Journal of the American Chemical Society*, 2023, 145 (5), pp.3108-3120. 10.1021/jacs.2c12336 . hal-04018519

HAL Id: hal-04018519

<https://cnrs.hal.science/hal-04018519>

Submitted on 7 Mar 2023

HAL is a multi-disciplinary open access archive for the deposit and dissemination of scientific research documents, whether they are published or not. The documents may come from teaching and research institutions in France or abroad, or from public or private research centers.

L'archive ouverte pluridisciplinaire **HAL**, est destinée au dépôt et à la diffusion de documents scientifiques de niveau recherche, publiés ou non, émanant des établissements d'enseignement et de recherche français ou étrangers, des laboratoires publics ou privés.

Doped Graphene to Mimic Bacterial NADH Oxidase for One-step NAD⁺ Supplementation in Mammals

Xi Liu¹, Jingkun Li², Andrea Zitolo³, Meng Gao¹, Jun Jiang¹, Xiangtian Geng⁴, Qianqian Xie¹, Di Wu¹, Huizhen Zheng¹, Xiaoming Cai⁴, Jianmei Lu⁵, Frédéric Jaouen^{*,6}, Ruibin Li^{*,1}

¹State Key Laboratory of Radiation Medicine and Protection, School for Radiological and Interdisciplinary Sciences (RAD-X), Collaborative Innovation Center of Radiological Medicine of Jiangsu Higher Education Institutions, Suzhou Medical College, Soochow University, Suzhou, 215123, China;

²School of Chemistry and Molecular Engineering, East China University of Science and Technology, Shanghai, 200237, China;

³Synchrotron SOLEIL, L'orme des Merisiers, BP 48 Saint Aubin, Gif-sur-Yvette, 91192, France;

⁴School of Public Health, Suzhou Medical College, Soochow University, Suzhou, 215123, China;

⁵College of Chemistry, Chemical Engineering and Materials Science, Soochow University, Suzhou, 215123, China

⁶ICGM, Univ. Montpellier, CNRS, ENSCM, Montpellier, 34293, France.

KEYWORDS. *Doped Graphene, Single Atom Catalyst, Nanotoxicity, Nanozyme, NAD⁺, NADH, Fe-N₄.*

ABSTRACT: Nicotinamide adenine dinucleotide (NAD) is a critical regulator of metabolic networks, and declining levels of its oxidized form, NAD⁺, are closely associated with numerous diseases. While supplementing cells with precursors needed for NAD⁺ synthesis has shown poor efficacy in combatting NAD⁺ decline, an alternative strategy is the development of synthetic materials that catalyze the oxidation of NADH into NAD⁺, thereby taking over the natural role of NADH oxidase (NOX) present in bacteria. Herein, we discovered that metal-nitrogen doped graphene (MNGR) materials can catalyze the oxidation of NADH into NAD⁺. Among MNGR materials with different transition metals, Fe-, Co- and Cu-NGR displayed strong catalytic activity combined with > 80% conversion of NADH into NAD⁺, similar specificity to NOX for abstracting hydrogen from the pyridine ring of nicotinamide, and higher selectivity than 51 other nanomaterials. The NOX-like activity of FeNGR functioned well in diverse cell lines. As a proof of concept of *in vivo* application, we showed that FeNGR could specifically target the liver and remedy the metabolic flux anomaly in obesity mice with NAD⁺-deficient cells. Overall, our study provides a distinct insight for exploration of drug candidates by design of synthetic materials to mimic the functions of unique enzymes (e.g., NOX) in bacteria.

INTRODUCTION

Nicotinamide adenine dinucleotide is an essential cofactor extensively expressed in all living cells¹. Its oxidized and reduced forms (NAD⁺ and NADH, respectively) play a key role in the electron transport chain of metabolic processes, where NAD⁺ serves as an electron acceptor in metabolic redox reactions of cells^{2,3}. These reactions are crucial for cells to maintain their elemental biological functions by harvesting energy from fuel molecules such as glucose and fatty acids⁴. The physiological functions of NAD⁺ as an essential coenzyme in metabolic networks have been highly underlined⁵. While the decline in NAD⁺ levels is closely associated with aging⁶, metabolic diseases^{7,8}, neurodegenerative disorders⁹ and cancers¹⁰,

¹¹, elevation of this cofactor by supplementing cells with precursors needed for NAD⁺ synthesis has shown considerable benefits in preclinical trials¹²⁻¹⁵. This has aroused great interest in the exploration of efficient and affordable pathways to increase NAD⁺ levels for biomedical applications.

Mammalian cells can produce NAD⁺ *via* two pathways, namely, the *de novo* synthesis (DNS) pathway and the salvage pathway¹⁶ (Figure S1). The former requires seven steps to synthesize NAD⁺ from its main building block, namely, the amino acid tryptophan, and was shown to be poorly efficient in biomedical applications¹⁷. The salvage pathway utilizes vitamin B₃ derivatives, including niacinamide (NAM), nicotinic acid (NA) or nicotinamide ribose (NR), bypassing the synthesis of adenine and resulting in the synthesis of NAD⁺ in

fewer steps¹⁸. However, supplementation of B₃ derivatives may lead to NADH accumulation, resulting in side effects such as hepatic pressure, tissue-specific cytotoxicity and even carcinogenesis¹⁹. In contrast to mammalian cells, a NADH oxidase (NOX) was found in some bacteria to be involved in the regulation of NAD⁺ levels *via* the direct conversion of NADH into NAD⁺²⁰. The advent of synthetic nanomaterials with NOX-like activity holds great interest.

The rapid development of nanotechnologies allows the precise design of nanostructures that mimic the catalytic properties of natural enzymes, namely, nanozymes^{21, 22}. However, most nanozymes can merely catalyse the degradation of peroxides, oxygen and superoxide, while nanozymes with reactivity toward C-H bonds have rarely been reported. Synthetic metal-nitrogen-graphene (MNGR) materials originally developed for catalyzing O₂ electroreduction were recently investigated in the field of heterogeneous catalysis for the activation of C-H bonds²³⁻²⁵. The 3d transition metals are often chosen as the dopants due to their superior efficiency to catalyze reduction and/or oxidation reactions, low toxicity and high abundance in the continental crust. An FeNGR material with single-metal-atom sites (Fe-N_x moieties) was shown to selectively catalyze the oxidation of a broad range of aromatic hydrocarbons into their corresponding ketones²³, and a CoNGR material with Co-N_x sites was reported to selectively catalyze the one-hydrogen abstraction from propane, resulting in propene²⁴. This ability of MNGR materials with M-N_x sites covalently embedded in graphene sheets to catalytically activate C-H bonds is in line with a similar ability reported for non-pyrolysed metal-phthalocyanines comprising a well-defined M-N₄ centre^{26, 27}. Metal-phthalocyanines are, however, less robust than MNGR single-atom catalysts, and their synthesis is more complex. Due to the reported activity of MNGR to activate C-H bonds selectively and efficiently, we hypothesized that they can be potential catalysts to mimic the activity of NOX for catalytic elevation of NAD⁺ in mammalian cells. While MNGR materials have recently been investigated as nanozymes with peroxidase- or catalase-like properties²⁸⁻³⁶, they have not yet been investigated as a NOX-like nanozyme to elevate NAD⁺.

Given that Fe, Mn, Zn, Cu and Co often serve as the catalytic core of many enzymes, we designed a series of MNGR materials by doping graphene with these transition metal and

nitrogen atoms to investigate their catalytic properties toward NADH oxidation (Figure S1). The catalytic products of NADH and O₂ in abiotic aqueous solutions were first examined by a colorimetric substrate, liquid chromatography and tandem mass spectrometry (LC-MS/MS). Among five synthetic MNGR materials, iron-, copper- and cobalt-doped NGR (FeNGR, CuNGR and CoNGR) were found to exhibit potent catalytic activity. Focusing on FeNGR due to iron's biocompatibility, the substrate selectivity, stability and kinetics of FeNGR were then extensively assessed under physiological conditions. The biological functions of FeNGR as an alternative to NOX were assessed in diverse mammalian cell lines and NAD⁺-deficient cell model by detecting the key intermediates in metabolic networks. Finally, as a proof of concept, the FeNGR material was exploited to remedy the metabolic flux anomaly in mice receiving high-fat diet (HFD). In summary, our study reports the discovery of the first nanozyme that mimics the catalytic properties of NOX from bacteria, with proven catalytic elevation of NAD⁺ levels in mammalian cells and animals.

RESULTS

Synthesis and Characterization of MNGR Materials. Five MNGR materials were prepared by changing only the nature of the transition metal in the synthesis. ZnNGR, CuNGR, CoNGR, FeNGR and MnNGR single-atom catalytic materials were prepared *via* flash pyrolysis at 1050 °C in flowing argon of dry-mixed metal acetate, 1,10-phenanthroline and ZIF-8, according to a method previously developed by us^{37, 38}. These materials were characterized by atomic force microscopy (AFM), Raman spectroscopy, X-ray diffraction (XRD), and X-ray absorption spectroscopy (XAS). The characterization data of Fe-, Cu- and Co-NGR, with high catalytic activity, are presented in the main manuscript, while those of Zn- and Mn-NGR (materials with lower activity) are presented in the supplementary materials.

The AFM images showed that the five MNGR materials had a lamellar structure consisting of a monolayer or a few atomic layers of carbon, with a thickness of 1.5-4.5 nm and a lateral size of 200-500 nm (Figure 1A and Figure S2A). The Raman spectra were similar for the five MNGR materials (Figure S3), revealing the G and D bands at 1583 and 1328 cm⁻¹ that are characteristic of the graphene plane and edges of

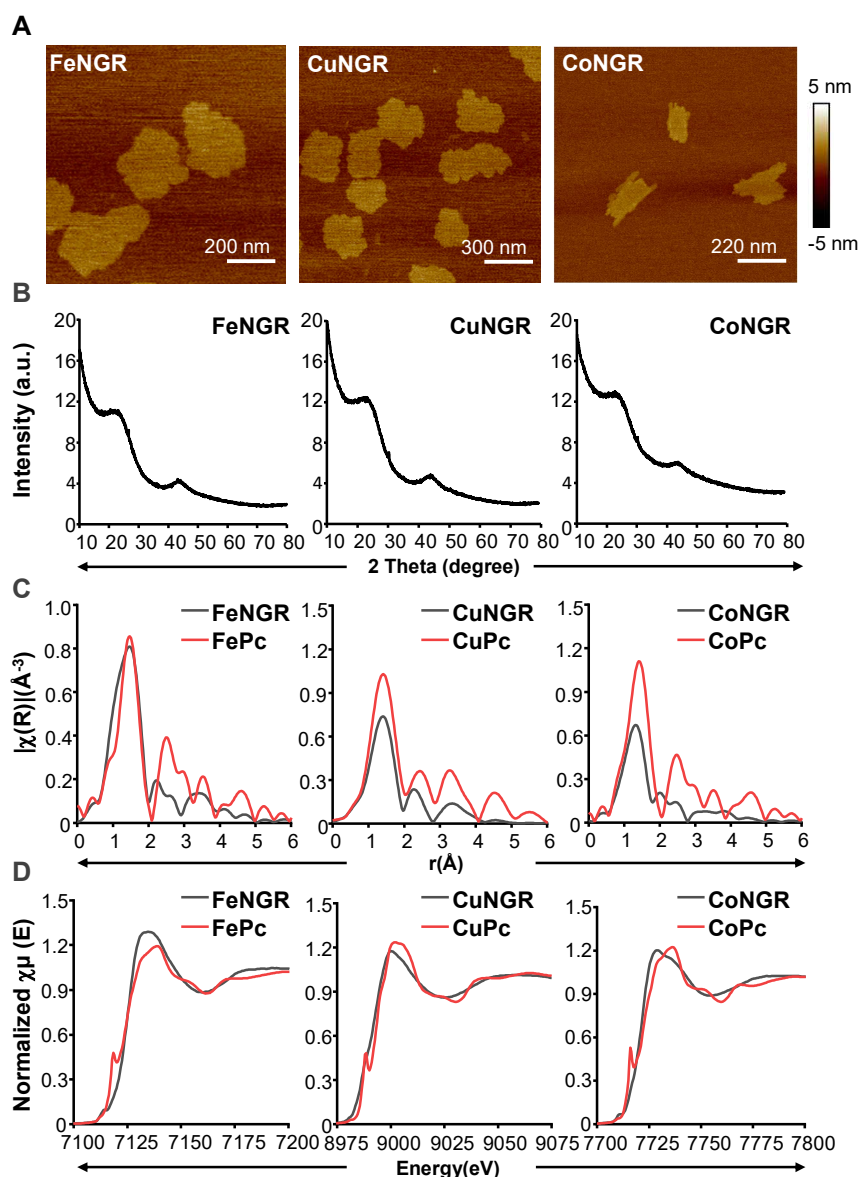


Figure 1. Characterization of MNGR materials. Characterization of the physicochemical properties of FeNGR, CuNGR and CoNGR by (A) AFM, (B) powder XRD patterns, (C) Fourier transformed EXAFS and (D) XANES spectra. A drop of MNGR material suspension at 50 $\mu\text{g/mL}$ was added to mica plates and dried at room temperature for AFM observation. Ten milligrams of MNGR powder were placed on silicon plates by direct compression for XRD. Pelletized MNGR powders bound with Teflon powder were used for EXAFS and XANES measurements at the metal K-edge. The EXAFS and XANES spectra for the respective metal-phthalocyanine compounds with well-defined metal- N_4 coordination are also shown (red curves in C and D).

small graphene planes, respectively³⁹. These results are in line with the small lateral size of graphene planes observed by AFM. Powder XRD showed only a first diffraction peak at *ca.* 22° that can be assigned to the reflection (002) of graphite and a second, broader peak at *ca.* 42° that can be assigned to the convoluted (100) and (101) reflections of graphite (Figure 1B and Figure S2B). The absence of diffraction peaks arising from crystalline metallic structures or other metal-rich crystal-

line structures in the as-prepared MNGR materials indicate that the metal atoms are likely atomically dispersed, as supported also by the extended X-ray absorption fine structure (EXAFS) analysis discussed below. The similar signatures of the carbon support in Raman spectra and XRD patterns for the five MNGR indicate that the NGR support is similar in all five materials, with the materials differing mainly in the nature of the metal dopant. We then resorted to XAS for identification

of the average local structure, and coordination environment of the transition metal in each MNGR material (Figure 1C-1D and Figure S2C). The Fourier transform (FT) of the EXAFS spectra of the MNGRs at their respective metal K-edge showed a major peak (~ 1.5 Å) and a secondary peak (2–3 Å). These two peaks can be attributed to the backscattering of light atoms (O, N, or C) situated in 1st and 2nd coordination spheres of the absorbing metal (Figure 1C). No strong M–M backscattering signal (expected at ~ 2 Å) was observed in the FT-EXAFS spectra, supporting the atomic dispersion of the metal centers in this series of MNGR materials. This is in line with previous characterizations on MNGR materials prepared identically by us, which have been extensively studied for various electrocatalytic applications⁴⁰.

M-N_x moieties (one central metal coordinated with multiple nitrogen atoms within one plane and possibly with additional axial oxygen ligand(s)) were then used as model structures to fit the metal K-edge EXAFS spectra. These model structures have successfully explained many structural features of MNGR materials with atomically dispersed transition metal sites achieved *via* pyrolysis^{38, 41}. The strong affinity of the metal for nitrogen is known to result in the spontaneous formation of stable M-N_x moieties at high temperature⁴². The proximity of metal and nitrogen atoms in MNGR was also experimentally supported with aberration-corrected scanning transmission electron microscopy⁴¹. The best-fit FT-EXAFS spectra obtained with such model sites showed an average coordination number of ~ 4 for Mn-, Co, Cu-, and ZnNGR, which supports the presence of in-plane M-N₄ moieties (Table S1). A higher overall coordination number of 5–6 was found for FeNGR, which again includes four nitrogen atoms in plane but also one or two axial ligands, likely oxygen ligands due to the high oxophilicity of Fe (Table S1). The results therefore indicate that the metal cations in MNGR are involved in an M-N₄ structure. These M-N₄ moieties are covalently embedded in-plane in graphene and resemble the square-planar M-N₄ structure of metal macrocycles such as metal-phthalocyanines (MPcs). This is supported by the analogous metal K-edge X-ray near edge absorption spectroscopy (XANES) spectra of MNGR and MPcs (Figure 1D and Figure S2D). The most prominent difference in the XANES spectra of MNGR and MPcs is the peak intensities of the pre-edge shoulder, which is

the characteristic feature of the square-planar M-N₄ structure. The negligible pre-edge shoulder in the XANES spectra of MNGR indicates that the M-N₄ moieties formed *via* pyrolysis are distorted, deviating from the well-defined square-planar M-N₄ geometry with four equal M-N bond lengths and four equal N-M-N bond angles in MPcs.

Assessment of the Catalytic Features of MNGRs. The MNGRs were subjected to reaction with aqueous NADH for examination of their catalytic activity by a colorimetric substrate, MTS (3-(4,5-dimethylthiazol-2-yl)-5-(3-carboxymethoxyphenyl)-2-(4-sulfophenyl)-2H-tetrazolium), which could rapidly react with NADH within 30 s, resulting in a color change from yellow to purple. This assay was exploited to acquire the standard curve of NADH, by which the percentages of NADH oxidized after a reaction time of 2 h were quantitatively determined by a calibration curve (Figure S4). As shown in Figure 2A, more than 80% NADH was converted after 2 h under catalysis by CoNGR, CuNGR and FeNGR, while MnNGR showed a moderate effect (62.8%), and merely 21.2% conversion was detected in the presence of ZnNGR. In contrast, undoped GR (prepared by ultrasonic exfoliation of graphite)⁴³ showed only *ca.* 5% conversion of NADH, indicating that M-N_x moieties in MNGRs account for their NOX-like catalytic activity rather than the graphene plane structure.

Given the high biocompatibility of iron over cobalt and copper dopants (Figure S5), FeNGR was selected for further exploration and application. To validate the catalytic activity assessed by the colorimetric assay, LC-MS/MS was used to directly detect the targeted catalytic product, NAD⁺. NADH and NAD⁺ standards were also included for comparison and showed distinct peaks at 2.45 min ($m/z = 666.1$ for NADH₂⁺) and 1.73 min ($m/z = 664.1$ for NAD⁺), respectively (Figure 2B). After the reaction of NADH with FeNGR, an intense peak assigned to NAD⁺ was detected, and no peak assigned to NADH was observed. Notably, FeNGR catalysis in a 2 h reaction time resulted in a high NAD⁺ yield (84.4%), which is similar to the effect (87.7%) of protein NOX (Figure 2C). To examine the catalytic kinetics of FeNGR towards the oxidation of NADH to NAD⁺, we measured the time dependence of NADH exhaustion online with a colorimetric assay under different initial concentrations of NADH. For comparison, the same experiments were carried out with NOX. As shown in

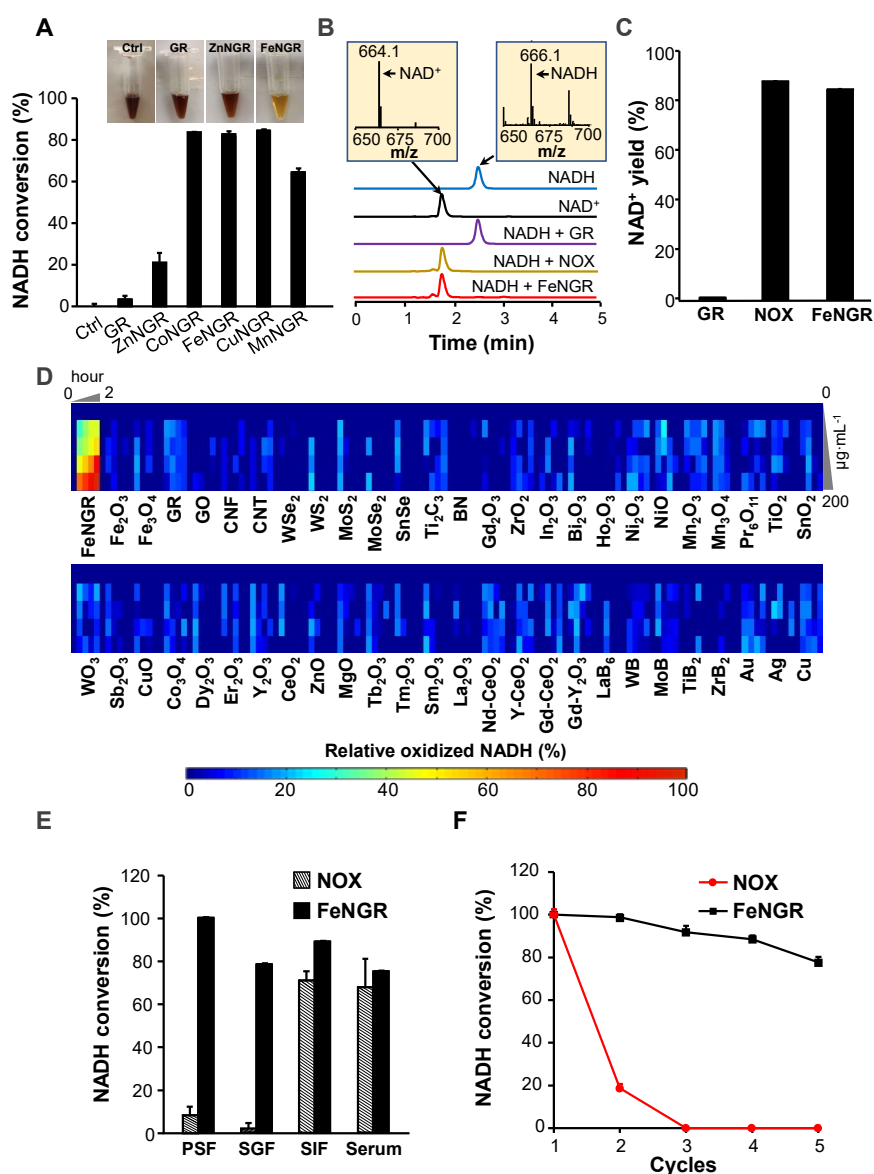


Figure 2. Abiotic assessment of the NOX-like activity of MNGRs. Assessment of catalytic activities of MNGR materials by (A) colorimetric assay and (B) LC-MS/MS. (C) NAD^+ yields in NADH oxidation reactions. Nanoparticles of MNGR at $200 \mu\text{g mL}^{-1}$ and NOX at 200mU mL^{-1} were used to react with NADH for 2 h in PBS (pH 7.4). The residual NADH amount was detected by MTS assay or LC-MS/MS ($n=3$ independent samples). For LC-MS/MS, the NAD^+ yield was calculated according to the following equation: NAD^+ yield (%) = $S_{\text{NAD}^+}/(S_{\text{NADH}} + S_{\text{NAD}^+}) \times 100\%$, where S_{NADH} and S_{NAD^+} represent the molar amounts of NADH and NAD^+ detected by LC-MS/MS, respectively. (D) Heatmap presenting dose (0- $200 \mu\text{g mL}^{-1}$) and time (0-2 h) responses of 52 nanomaterials towards the catalysis of NADH oxidation. The catalytic activities were assessed by the absorbance changes of the substrate in the MTS assay (see supplementary material, methods section: *Assessment of NOX-like activity by colorimetric assay*). (E) Comparisons of the stability of FeNGR and NOX in four simulated biofluids. FeNGR ($200 \mu\text{g/mL}$) and NOX (200mU/mL) were pretreated in phagolysosomal simulated fluid (PSF), simulated gastric fluid (SGF), simulated intestinal fluid (SIF) and serum for 2 h. The catalytic activities of treated FeNGR or NOX were detected by MTS assay ($n=3$ independent samples). (F) Durability of FeNGR and NOX. An ultrafiltration membrane was used to separate FeNGR and NOX after each NADH oxidation reaction cycle. The catalytic activity before each cycle was measured by MTS assay ($n=3$ independent samples).

Figure S6, the kinetic curves of NADH oxidation catalyzed by FeNGR and NOX could both be fitted by the Michaelis-Menten equation:

$$v = V_{max} \times [S] / (K_m + [S])$$

where $[S]$ is the concentration of substrate, K_m is the Michaelis constant, V_{max} is the maximum rate, and v is the initial rate for a given $[S]$. The NADH oxidation catalyzed by FeNGR and NOX has similar kinetic constants, with V_{max} values of 2.5×10^{-2} and $4.1 \times 10^{-3} \text{ mM}\cdot\text{s}^{-1}$ and Michaelis constants of *ca* 3.97 and 0.35 mM, respectively (Figure S6). We exploited the V_{max} values to calculate the average single-site activity of catalytic sites in FeNGR (Fe-N₄) and compared it to the active site in NOX (tryptophan 47 domain). While the quantification of the number of active sites with a cyanide molecular probe indicated that the Fe-N₄ site density on the top surface in this FeNGR is *ca.* 3.3×10^{19} sites/g⁴⁴, the number of catalytic domains in NOX can be assessed from its known molecular weight to be 1.12×10^{19} sites/g (see supplementary material, methods section: *Detection of catalytic reaction kinetics*). As a result, after normalization by the number of sites in presence during the catalytic test, the single-site activity of FeNGR is 2.4 mole of NAD⁺ per mole of Fe-N₄ sites and per second, while the single-site activity of NOX is *ca* 5.5 mole of NAD⁺ per mole of tryptophan 47 domains and per second (see supplementary material, methods section: *Detection of catalytic reaction kinetics*).

With the colorimetric assay, we then benchmarked the NOX-like catalytic activity of FeNGR to a pool of 52 synthetic nanomaterials covering 39 chemical elements, 17 crystal phases and 6 morphologies (Figure 2D, Table S2). For a snapshot view of the results, the measured absorbance values after 2 h of reaction time were ranked into three levels, leading to a visual display where high, moderate and negligible levels of NADH oxidation are represented by red, yellow and blue colors, respectively (Figure 2D). Interestingly, only FeNGR displayed dose- and time-dependent catalytic activity among all 52 tested materials, indicating good catalytic selectivity. Moreover, FeNGR specifically catalyzed hydrogen abstraction from the 1, 4-dihydropyridine-3-carboxamide and had little effect on hydrogens in the benzene, quinoline, pyran and pyrimidine rings (Table S3). These results suggest that FeNGR is a NOX-like nanozyme, displaying the prominent features of

enzymes⁴⁵, including high catalytic efficiency under physiological conditions, catalytic specificity and substrate selectivity.

Stability of FeNGR in NADH Oxidation. In biological systems, FeNGR may cross diverse biological contexts in tissues or subcellular compartments, such as blood vessels, gastric intestine, and phagolysosomes, to reach the destinations for interaction with NADH. We therefore examined the stability of FeNGR in four representative harsh bio-contexts, including simulated gastric fluid (SGF), serum, simulated intestinal fluid (SIF), and phagolysosomal simulated fluid (PSF). FeNGR or NOX immersed in these fluids for 2 h at 37 °C was subjected to a catalytic activity test and compared with the activity of untreated materials. Notably, FeNGR displayed high stability in all these media, maintaining > 70% catalytic activity (Figure 2E). The strongest decrease in activity was after immersion in SGF (pH 1.2), corresponding to the lowest pH of all four simulated bio-fluids, and may be due to the leaching of Fe cations from FeNGR in a strongly acidic medium. In contrast, NOX was more sensitive to digestive acidic fluids, retaining only 9.04 and 1.7% activity after exposure to PSF and SGF, respectively, which could be attributed to the acidic pH effect. Moreover, compared to NOX, FeNGR had stable catalytic activity (>75%) over a wide range of temperature at 4-90 °C, ion strength at 0.5-3.0 M or pH at 4-8.

In addition, we examined the durability of FeNGR by separating it from the reaction system after 2 h and re-introducing it into a fresh reaction solution for catalysis. This recycling procedure was repeated several times. As shown in Figure 2F, the catalytic activity of FeNGR slightly decreased from the first to the second cycle and preserved > 80% of its initial catalytic activity after four cycles, whereas natural NOX lost 81.2% activity on the second cycle and was completely inactivated on the third cycle. These results indicate that FeNGR is more robust to degradation by biological media and displays superior durability, which may enable a long-lasting elevation of NAD⁺ levels in cells.

Catalytic Elevation of NAD⁺ in Cells. To increase cellular NAD⁺ levels by FeNGR catalysis, the impact of FeNGR on cell growth was first examined to determine a safe dose range. Cell viability tests indicated that FeNGR has high biocompatibility over a broad concentration range (0-200 µg/mL) (Figure

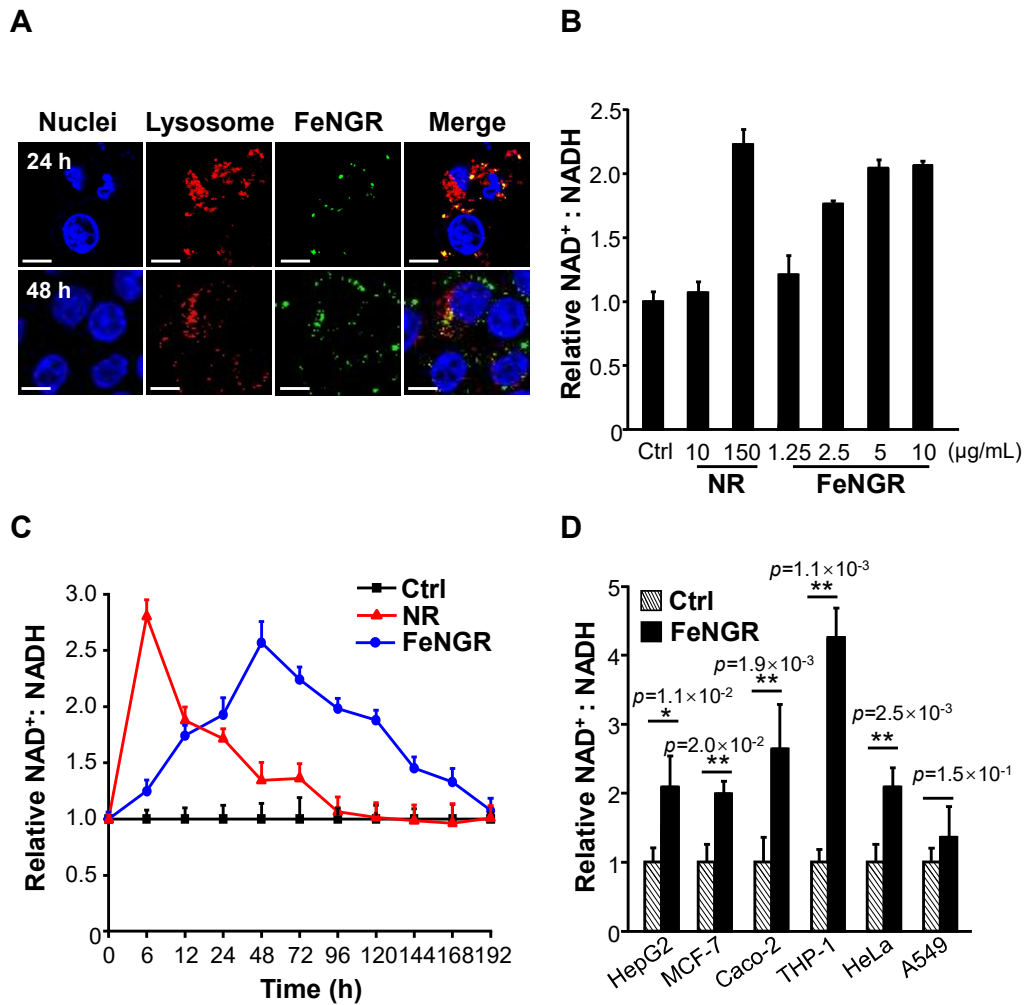


Figure 3. Validation of the catalytic activity of FeNGR in cells. (A) Representative confocal images of FeNGR in cells. FeNGR was labelled by FITC conjugated with BSA and denoted as FITC-FeNGR (green). HepG2 cells treated with 10 µg/mL FeNGR for 24 and 48 h were stained with Hoechst 33342 (blue) and anti-LAMP1 (red) to visualize the nuclei and lysosome in cells, respectively (scale bar, 10 µm). Enzymatic activity of FeNGR in HepG2 cells at (B) different concentrations and (C) different incubation times. HepG2 cells were treated with different concentrations of FeNGR (0-10 µg/mL) or NR (10-150 µg/mL) for 24 h (B) or with 10 µg/mL FeNGR and 150 µg/mL NR for 0-192 h. (C). The treated cells were collected and lysed to detect the ratios of NAD⁺/NADH by an Amplite™ Fluorimetric NAD/NADH ratio assay kit (n = 3 biologically independent cell samples). (D) Catalytic activity of FeNGR in different cell lines. HepG2, MCF-7, Caco-2, THP-1, HeLa and A549 cells were exposed to 10 µg/mL FeNGR for 24 h. Then, the cells were collected and lysed to detect NAD⁺ and NADH by an Amplite™ Fluorimetric NAD/NADH ratio assay kit (n = 3 biologically independent cell samples). The NAD⁺/NADH ratios reported in this figure are normalized to the value measured for NAD⁺/NADH for either the control (B and D) or at time 0 (C). * p<0.05, **p<0.01 and *** p<0.001 compared to control cells by two tailed Student t-test.

S7). Since the cytoplasm is an important reservoir of NADH, we examined whether FeNGR could be internalized into this cellular compartment. Fluorescein isothiocyanate labeled FeNGR (FITC-FeNGR) was prepared for confocal microscopy imaging of cellular distributions. FeNGR showed a time-dependent distribution pattern, including association with cytoplasmic membranes at 0-6 h, lysosomal internalization at 6-

24 h, and release into the cytoplasm after 24 h (Figure 3A and S8). The coincident settlement of NADH and FeNGR in the cytoplasm provided an essential prerequisite for the catalytic oxidation of NADH into NAD⁺ from the perspective of spatial distributions. A high NAD⁺ yield was therefore expected in cells after incubation with FeNGR for more than 24 h. To examine this, we assessed the ratios of NAD⁺ to NADH in

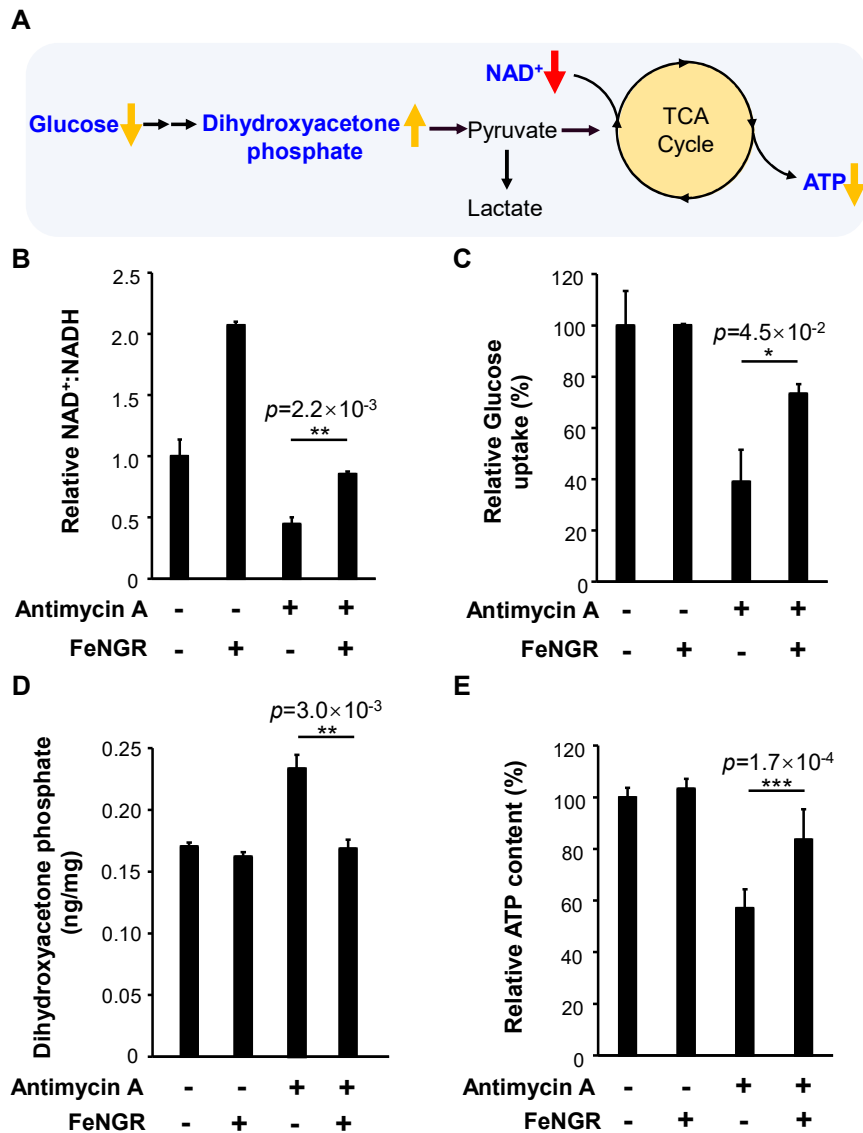


Figure 4. Effects of FeNGR in ETC-deficient cells. (A) Scheme showing key changes in metabolite levels in ETC-deficient cells. (B) The intracellular NAD⁺/NADH ratio, (C) glucose uptake, (D) dihydroxyacetone phosphate accumulation and (E) ATP generation in ETC-deficient HepG2 cells with or without FeNGR treatment. The ETC-deficient HepG2 cell model was established by 2 μ M antimycin A treatment, denoted as antimycin A + in figure B-E. Antimycin A – indicates normal HepG2 cells. Parent and ETC-deficient cells were incubated with 10 μ g/mL FeNGR for 72 h before measurement of the NAD⁺/NADH ratio and dihydroxyacetone phosphate by LC–MS/MS as well as ATP production by Celltiter Glo luminescent cell viability assay. Data are presented as the mean \pm S.D. (n = 3 biologically independent cell samples). * $p < 0.05$, ** $p < 0.01$ and *** $p < 0.001$ compared to ETC-deficient cells by two tailed Student t-test.

HepG2 cells exposed to FeNGR. As shown in Figure 3B and C, FeNGR displayed time- and dose-dependent catalytic effects in elevating the NAD⁺/NADH ratios, which reached a maximum in cells after 36 h of incubation with 10 μ g/mL FeNGR nanosheets, decreasing slowly afterwards. Notably, at the same mass concentration (10 μ g/mL), nicotinamide riboside (NR), a conventional precursor for NAD⁺ supplementa-

tion, had no effect on NAD⁺ production. Compared to the effect with NR at a concentration of 150 μ g/mL (*i.e.*, a 15-fold higher dose compared to FeNGR), FeNGR contributed to a longer supplementation of NAD⁺ with 1.8-fold higher total NAD⁺ production in HepG2 cells for 8 d incubation time, whereas the effect of NR rapidly dropped by 50% in 24 h (Figure 3C) In addition to the investigation with hepatic cells,

we extensively examined the catalytic effects of FeNGR in more cell lines, including intestinal (Caco-2), monocyte (THP-1), breast (MCF-7), cervical (HeLa) and pulmonary (A549) cells. As shown in Figure 3D, cellular internalization of FeNGR significantly elevated the NAD^+/NADH ratios in five tested cell lines, except for A549 cells. Notably, the NAD^+/NADH ratios increased 4.2-fold in THP-1 cells. This is not surprising because the primed THP-1 cells have macrophage-like features and often take in more nanomaterials than other cells⁴⁶. All these results demonstrate that FeNGR efficiently catalyzes the conversion of NADH into NAD^+ in a complex intracellular environment.

Assessment of the Biological Function of FeNGR in ETC-Deficient Cells. Given that the conversion of NADH into NAD^+ is determined by the mitochondrial electron transport chain (ETC) in mammalian cells, we further examined the biological function of FeNGR in ETC-deficient cells, which are often associated with metabolic diseases (*e.g.*, adiposity and diabetes)^{47,48} and are featured by insufficient supplementation of NAD^+ . The mitochondrial ETC dysfunction model was established in HepG2 cells by antimycin A treatment to inhibit mitochondrial complex III. Since NAD^+ is a critical cofactor in oxidation-phosphorylation metabolic pathways, failure of NAD^+ supplementation may result in the decline of glucose uptake, ATP deficiency or accumulation of intermediates (*e.g.*, dihydroxyacetone phosphate, glyceraldehyde 3-phosphate or pyruvic acid) in the metabolic network (Figure 4A).

As shown in Figure 4B, compared to parent HepG2 cells, the ETC-dysfunctional cells displayed a 55.5% decrease in the $\text{NAD}^+:\text{NADH}$ ratio. Accordingly, glucose uptake and ATP production reduced by 60.9% and 42.0%, respectively (compare the 1st and 3rd columns in Figure 4C and 4E). In contrast, dihydroxyacetone phosphate, an important intermediate that is rapidly exhausted in the natural glycolysis pathway, showed a 35.5% increase (compare the 1st and 3rd columns in Figure 4D). These data confirm the successful construction of ETC-deficient cell models. Exposure of such cells to FeNGR significantly elevated the relative ratio of NAD^+/NADH from 0.4 to 0.9 (compare the 3rd and 4th columns in Figure 4B). Consequently, there were 88.0%, 27.0% and 49.1% increments of glucose uptake, dihydroxyacetone phosphate consumption and

ATP production, respectively, in ETC-deficient cells after FeNGR treatment (compare the 3rd and 4th columns in Figure 4C, D, E). Interestingly, although the uptake of FeNGR in normal HepG2 cells induced a significant increase in the NAD^+/NADH ratio, it had negligible effects on the glucose, dihydroxyacetone phosphate and ATP levels. These results demonstrate that FeNGR helps recovering the metabolism of ETC-deficient cells by catalytic elevation of NAD^+ .

Catalytic Elevation of NAD^+ in Mice with Metabolic Diseases. In animals, the liver is the core organ to metabolize lipid, carbohydrate and protein. Defective hepatic metabolism has been found to be responsible for severe diseases such as adiposity and diabetes. As a proof of concept for the biomedical application of FeNGR, we explored the possibility of elevating NAD^+ levels in the livers of mice subjected to a high-fat diet (HFD). First, we examined whether FeNGR could target this organ. Radio- and fluorophore-labelled FeNGR (¹²⁵I-FeNGR and FITC-FeNGR) were prepared to examine the biodistribution by single photon emission computed tomography-computed tomography (SPECT-CT) or confocal microscopy. More than 98.8% labeled FeNGR stably present in a representative biological medium, serum (Figure S9). After intravenous injection of ¹²⁵I-FeNGR dispersed in PBS, a large portion of ¹²⁵I-FeNGR rapidly targeted the liver within 6 h and was retained there for 7 days (Figure 5A). Although corona formation on FeNGR surfaces (Table S6) may affect the catalytic activity, FeNGR maintained > 70% activity in serum over 9 d exposure (Figure S10).

Confocal microscopy further revealed the distribution details in liver tissue sections. As shown in Figure 5B, the uptake of FeNGR was mainly by hepatocytes and Kupffer cells, both of which play important roles in hepatic metabolic processes. The long hepatic bio-persistence and strong cellular internalization capability of FeNGR offered opportunities for catalytic elevation of NAD^+ in the liver. Meanwhile, the H&E staining images of tissues as well as blood test results showed negligible detrimental effects (Figure S11 and Table S4).

We then examined the effects of FeNGR injected to HFD-fed mice *via* tail vein. Animals that received a chow diet (CD) were also included for comparison. Significant glucose tolerance was detected in HFD mice after 12 weeks of feeding. Then, the HFD mice were subjected to intravenous injection of

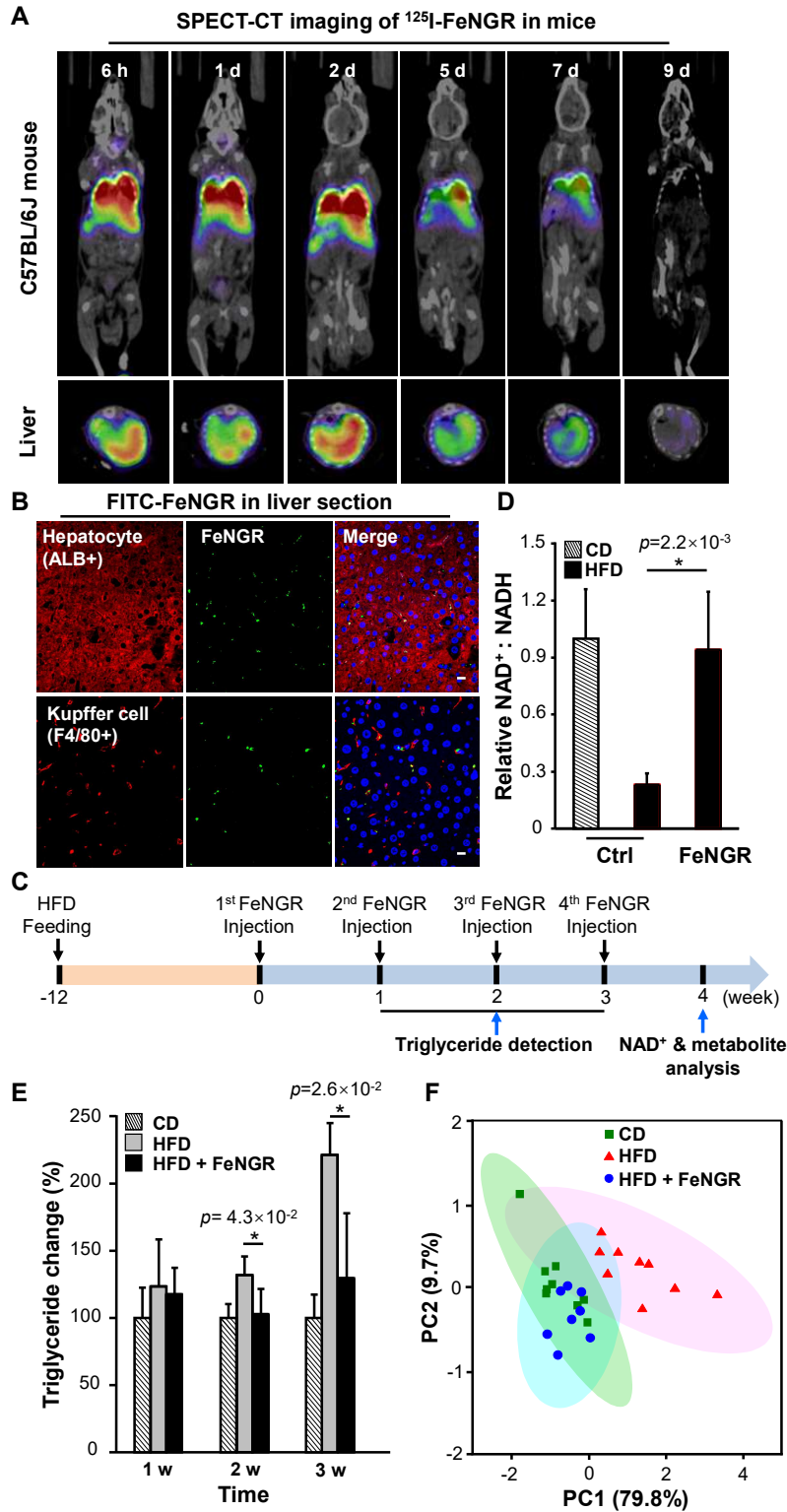


Figure 5. Effect of FeNGR in HFD mice. (A) SPECT/CT imaging of ^{125}I -FeNGR in mice and **(B)** confocal imaging of FITC-FeNGR in liver sections. Mice were exposed to 10 mg/kg ^{125}I -FeNGR or FITC-FeNGR by tail vein injection. ^{125}I -FeNGR in mice was visualized by SPECT-CT (IVIS spectrum, MILabs, Netherlands) for 9 days. Mice that received FITC-FeNGR injection were sacrificed at 24 h to collect livers for fixation in formaldehyde solution and preparation of liver sections. The hepatocytes and Kupffer cells in liver sections were stained with Cy3-labelled albumin and F4/80 antibodies (red), respectively. Cell nuclei were stained with DAPI (blue). The stained sections were visualized by confocal microscopy imaging. **(C)** Schematic image of animal treatment procedure. **(D)** Hepatic NAD^+/NADH

ratios (n= 6 independent animal samples) and (E) blood triglyceride levels in treated and untreated mice (n= 6 independent animal samples). (F) PCA of the serum metabolites from CD (n = 9 independent animal samples), HFD (n = 9 independent animal samples) and FeNGR-HFD mice (n= 8 independent animal samples). Animals that received an intravenous injection of PBS or 10 mg/kg FeNGR were sacrificed on the 28th day to collect blood and livers for metabolite analysis by LC–MS/MS. * p< 0.05, **p< 0.01 and *** p< 0.001 compared to HFD mice by two tailored Student t-test.

FeNGR, denoted as the FeNGR-HFD group. The dose-response curve showed that FeNGR at ≥ 10 mg/kg could greatly promote the glucose metabolism rate (Figure S12). Therefore, the HFD mice were treated four times with FeNGR at this dose in each 7 day interval. The detailed animal treatment procedure is illustrated in Figure 5C. As shown in Figure 5D, intravenous injection of FeNGR in HFD mice greatly mitigated the decline in NAD⁺/NADH triggered by HFD, with a 4.1-fold higher NAD⁺/NADH ratio after 4 weeks compared to untreated HFD mice, displaying a NAD⁺/NADH ratio similar to that of CD mice. While HFD feeding resulted in a significant decline in NAD⁺/NADH ratios in mouse liver, lipid metabolism was affected accordingly, as evidenced by 2-fold higher serum triglycerides, compared to the results in CD mice (compare diagonal-line-filled and gray columns at week 3, in Figure 5E)

Triglyceride is mainly metabolized in liver by lipase into glycerin and fatty acids. While glycerin could be further converted into dihydroxyacetone phosphate by glycerol kinase (GK) and glycerophosphate dehydrogenase (GPDH) with the assistance of NAD⁺, fatty acids were metabolized by TCA cycle along with the consumption of NAD⁺ (Figure S13). Supposedly, elevation of hepatic NAD⁺/NADH by FeNGR could enhance the metabolic rate of triglyceride. Accordingly, the FeNGR injection contributed to a significant decrease (41.4%) in triglyceride levels at three weeks as well as relieving insulin resistance (Figure S14). These data indicate that the administration of FeNGR may mitigate metabolic anomalies in HFD mice.

To validate this, we exploited non-target metabolomics to screen the levels of metabolites in serum samples from CD, HFD and FeNGR-HFD mice. LC–MS/MS analysis identified 1295 confident features in all three groups. The metabolite features were subjected to a clustering analysis for calculation of the Euclidean distance (ED) between the FeNGR-HFD and CD groups, and the HFD and CD groups. Essentially, ED is a suitable index to assess the overall effect of FeNGR on HFD

mice, with a shorter ED indicating fewer metabolic anomalies. As shown in Table S5, administration of FeNGR to HFD mice resulted in a 2.7-fold decrease in the ED value compared to HFD mice. Principal component analysis (PCA) was also exploited to assess the differences in metabolite expression among the CD (green square), HFD (red triangle) and FeNGR-HFD (blue circle) groups (Figure 5F). The maximum number of PCs was set to 26 for the analysis. As shown in Figure 5F, the cumulative contribution of the first two principal components to the total variance was 89.5%. The PCA plot showed that the HFD group was clearly distinct from the CD group. Interestingly, after FeNGR treatment, the metabolite levels of HFD mice were normal in six out of eight HFD mice, as revealed by their distribution in the green region of the CD group. These results suggest that FeNGR administration could relieve the metabolic disorder of HFD-fed mice.

DISCUSSION

The elevation of NAD⁺ level has considerable benefits in regulating metabolic flux of mammals. To supplement NAD⁺ in mammals, biological researcher has raised two approaches, namely the natural synthesis and catalytic conversion. According to the synthesis pathway of NAD⁺, a few intermediates including NAM⁴⁹, NA⁵⁰ and NR⁵¹ have been exploited to elevate NAD⁺ levels, bypassing the synthesis of adenine from the main building block, tryptophan. Besides, Mootha's group attempted to further improve the supplement efficiency by engineering protein enzymes, including combined enzymes consisting of bacterial lactate oxidase (LOX) and catalase (CAT) and bacterial water-forming NADH oxidase (NOX)^{52, 53}, for the catalytical elevation of NAD⁺ in cells. To the best of our knowledge, chemical approaches were rarely developed to increase NAD⁺ levels. Given the shortcomings of protein enzymes, such as poor cellular internalizations, low stability in harsh biological fluids, and high cost to scale up, we engineered a synthetic material to mimic the activity of bacterial NOX and elevate NAD⁺ in mammals.

Biosafety is a paramount issue in terms of the clinical translation of nanomedicine and is often controversial^{54, 55}. Recent studies indicate that nanomaterials could be designed by tuning their physicochemical properties to acquire desired biological effects⁵⁶⁻⁵⁸. Although Co, Cu- and Fe-NGRs showed similar NOX-like activity, FeNGR was selected for further exploration in cells and animals because iron is abundantly expressed in biological systems and relatively safe compared to the other two metals. FeNGR was coated with lipidated polyethylene glycol to improve dispersion stability.

The biodistribution and clearance of FeNGR in mice were examined by SPECT/CT after radiolabelling. Consistent with a literature report⁵⁹, the intravenously injected FeNGR rapidly targeted the liver in 6 h, and most of the FeNGR was eliminated in 9 days. The biological fate of nanomaterials is largely determined by their morphology and surface corona⁶⁰. For instance, the comparison of MoS₂ biodistribution in transgenic mice with fibrinogen (Fg), apolipoprotein E (ApoE), immunoglobulin M (IgM) or complement 3 (C3) deficiency provides convincing support that ApoE binding on MoS₂ nanosheets dictates their accumulation in liver sinusoid and splenic red pulp^{61, 62}. In this study, twelve apolipoproteins were identified in the 320 corona proteins of FeNGR (Table S6). Given that FeNGR has similar planar structure with MoS₂ nanosheets, we speculated that the excellent liver targeting of FeNGR could be attributed to the constituent of apolipoproteins in surface corona. There might be two mechanisms dictating the clearance of FeNGR *in vivo*. On the one hand, the intravenously injected graphene sheets were reported to be eliminated by both fecal and urinary excretions⁵⁹; on the other hand, enzymes including peroxidases were demonstrated to catalyze the biodegradation of graphene derivatives^{63, 64}. Moreover, we examined the possible pathogenic changes in tissue sections and biochemical indicators in blood from mice receiving intravenous injection of FeNGR. Although the numbers of white blood cells and lymphocytes showed slight increases on the 1st day, they all recovered on the 7th day. H&E staining images of heart, liver, spleen, kidney and lung showed no pathogenic changes. To further minimize the risks of detrimental effects in humans from exposure and facilitate the clinical translation of MNGR, the candidate materials should be engineered in a

colloidal dispersion state with small-sized individual graphene sheets and hydrophilic groups on surfaces.

Two mechanisms, *i.e.*, coupled electrochemical reaction (CER) and inner-sphere reaction (ISR) have been raised to explain the oxidation reactions catalyzed by MNGRs^{65, 66}. The CER mechanism could be interpreted as two coupled electrochemical reactions, one for O₂ electro-reduction and the other for the substrate electro-oxidation, the coupled half-reactions working formally as a short-circuited electrochemical cell. In this view, a better O₂ reduction catalyst then results in a higher driving force for the electrooxidation of the organic molecule. In contrast, Bates et al proposed that the aerobic oxidation of substrate on MNGR materials is not the sum of two independent electrochemical half-reactions, but rather a direct inner-sphere reaction between O₂ and the organic molecule⁶⁷. In this mechanism, O₂ and the organic molecules co-adsorb on the metal center of the MNGR surface. As a result, the best catalyst for O₂ reduction will not necessarily be the most active one for aerobic oxidation of an organic molecule. Nevertheless, whether the CER or ISR mechanism dictates the NADH oxidation, the MNGR catalyst must have the ability to bind and activate O₂. As such, the Co-, Cu- and FeNGR types of materials are known to be far more active towards O₂ electro-reduction than ZnNGR and MnNGR⁶⁸, and thus their higher activity and selectivity in the present study towards NADH oxidation can be rationally explained, according to either of these mechanisms.

While the activity for oxidation of NADH into NAD⁺ normalized per active site is *ca.* 2 times lower for the present FeNGR than for NOX, the number of active sites per mass of catalyst is *ca.* 3 times higher for the present FeNGR than for NOX, resulting in comparable effects at the same dose. In the future, optimized syntheses can improve the activity of FeNGR *via* increased site density, improved site-specific activity, and tuned catalyst morphology. A recent work has shown that FeNGR materials with a site density of 1.9×10^{20} sites/gram can be prepared, *ca.* 6 times higher than in the present FeNGR⁶⁹. Although Fe₂O₃ has been observed *operando* from FeNGR degradation in proton exchange membrane fuel cell, Fe₂O₃ is poorly reactive toward NADH oxidation (Figure 2D), indicating that FeN₄ is the true active site. The site-specific activity of FeNGR materials might also be improved

by the selective formation of Fe-N_x sites with a specific oxidation state and spin state (while the present FeNGR has two main Fe-N_x species, differing both in their Fe oxidation and spin states) or by co-doping the carbon matrix with nitrogen and another light element, such as sulfur⁷⁰. Finally, the catalyst morphology may also play an important role for *in vivo* applications, including effects on the rate of cellular internalization of FeNGR and its elimination from the body. While commercial ZIF-8 was used to prepare the present FeNGR, the synthesis of ZIF-8 with a controlled crystal size is well established (from 30 to 1600 nm) and was shown to translate into precise control of the size of FeNGR particles after pyrolysis^{71, 72}.

CONCLUSIONS

In summary, synthetic CuNGR, FeNGR and CoNGR nanosheets showed significant NOX-like activity. Compared to natural NOX, FeNGR is more robust to four representative biological fluids. FeNGR could be internalized into the cytoplasm to elevate NAD⁺/NADH ratios, contributing to increments of glucose uptake and ATP production, in ETC-deficient cells. Intravenously injected FeNGR could target livers internalized by hepatic and Kupffer cells and enabled 4.1-fold increases in the NAD⁺/NADH ratio in the liver tissue of HFD-fed mice. The serum metabolite profiles demonstrated a dramatic relief of metabolic disorders in HFD-fed mice. Taken together, the discovery of MNGR as a NOX-like catalyst provides a promising approach to regulate metabolic flux by the rational design of synthetic nanomaterials. FeNGR and other MNGR could potentially be exploited to treat some metabolic disorders, such as diabetes, fatty liver and hyperlipemia.

ASSOCIATED CONTENT

Supporting Information. The Supporting Information is available free of charge at <http://pubs.acs.org>.

Experimental procedures, statistical method, Raman, AFM, EXAFS, XANES, K-Edge FT-EXAFS Spectra, kinetics of reaction, catalytic activity with different substrate, cell viability histological H&E staining images, glucose sensitivity, insulin sensitivity and blood test data (PDF).

AUTHOR INFORMATION

Corresponding Author

Ruibin Li - State Key Laboratory of Radiation Medicine and Protection, School for Radiological and Interdisciplinary Sciences (RAD-X), Collaborative Innovation Center of Radiological Medicine of Jiangsu Higher Education Institutions, Suzhou Medical College, Soochow University, Suzhou 215123, Jiangsu China; Email: liruubin@suda.edu.cn

Frédéric Jaouen - ICGM, Univ. Montpellier, CNRS, ENSCM, Montpellier, France; Email: frederic.jaouen@umontpellier.fr
Notes

The authors declare no competing financial interest.

ACKNOWLEDGMENT

This work was supported by grants from the National Key R&D Program of China, Ministry of Science and Technology of China (2020YFA0710700, 2022YFE0124000), the National Natural Science Foundation of China (21976126), the Natural Science Foundation of Jiangsu Province (BK20211545), and the Project of National Center for International Research on Intelligent Nano-Materials and Detection Technology in Environmental Protection, Soochow University (No. SDGH2202). We acknowledge Synchrotron SOLEIL (Gif-sur Yvette, France) for provision of synchrotron radiation facilities at beamline SAMBA (proposal number 20180635)

REFERENCES

- (1) Zapata-Perez, R.; Wanders, R. J. A.; van Karnebeek, C. D. M.; Houtkooper, R. H. NAD⁺ homeostasis in human health and disease. *Embo Mol. Med.* **2021**, *1* (7), e13943.
- (2) Kim, W.; Deik, A.; Gonzalez, C.; Elena Gonzalez, M.; Fu, F.; Ferrari, M.; Churchhouse, C. L.; Florez, J. C.; Jacobs, S. B. R.; Clish, C. B.; Rhee, E. P. Polyunsaturated fatty acid desaturation is a mechanism for glycolytic NAD⁺ recycling. *Cell Metab.* **2019**, *29* (4), 856-870.
- (3) Palzer, L.; Bader, J. J.; Angel, F.; Witzel, M.; Blaser, S.; McNeil, A.; Wandersee, M. K.; Leu, N. A.; Lengner, C. J.; Cho, C. E.; Welch, K. D.; Kirkland, J. B.; Meyer, R. G.; Meyer-Ficca, M. L. Alpha-amino-beta-carboxy-muconate-semialdehyde decarboxylase controls dietary niacin requirements for NAD⁺ synthesis. *Cell Rep.* **2018**, *25* (5), 1359-1370.
- (4) Roichman, A.; Elhanati, S.; Aon, M. A.; Abramovich, I.; Di Francesco, A.; Shahar, Y.; Avivi, M. Y.; Shurgi, M.; Rubinstein, A.; Wiesner, Y.; Shuchami, A.; Petrover, Z.; Lebenthal-Loinger, I.; Yaron, O.; Lyashkov, A.; Ubaida-Mohien, C.; Kanfi, Y.; Lerrer, B.; Fernandez-Marcos, P. J.; Serrano, M.; Gottlieb, E.; de Cabo, R.;

- Cohen, H. Y. Restoration of energy homeostasis by SIRT6 extends healthy lifespan. *Nat. Commun.* **2021**, *12* (1), 3208.
- (5) Ralto, K. M.; Rhee, E. P.; Parikh, S. M. NAD⁺ homeostasis in renal health and disease. *Nat. Rev. Nephrol.* **2020**, *16* (2), 99-111.
- (6) Zhang, H.; Ryu, D.; Wu, Y.; Gariani, K.; Wang, X.; Luan, P.; D'Amico, D.; Ropelle, E. R.; Lutolf, M. P.; Aebersold, R.; Schoonjans, K.; Menzies, K. J.; Auwerx, J. NAD⁺ repletion improves mitochondrial and stem cell function and enhances life span in mice. *Science* **2016**, *352* (6292), 1436-1443.
- (7) Samuel, V. T.; Shulman, G. I. Nonalcoholic fatty liver disease as a nexus of metabolic and hepatic diseases. *Cell Metab.* **2018**, *27* (1), 22-41.
- (8) A Hand, G.; N Blair, S. Energy flux and its role in obesity and metabolic disease. *Endocrinology* **2014**, *10* (2), 131-135.
- (9) Kapogiannis, D.; Mattson, M. P. Disrupted energy metabolism and neuronal circuit dysfunction in cognitive impairment and Alzheimer's disease. *Lancet Neurol.* **2011**, *10* (2), 187-198.
- (10) DeBerardinis, R. J.; Thompson, C. B. Cellular metabolism and disease: What do metabolic outliers teach us? *Cell* **2012**, *148* (6), 1132-1144.
- (11) Schwartz, J.-M.; Otokuni, H.; Akutsu, T.; Nacher, J. C. Probabilistic controllability approach to metabolic fluxes in normal and cancer tissues. *Nat. Commun.* **2019**, *10* (1), 2725.
- (12) Titov, D. V.; Cracan, V.; Goodman, R. P.; Peng, J.; Grabarek, Z.; Mootha, V. K. Complementation of mitochondrial electron transport chain by manipulation of the NAD(+)/NADH ratio. *Science* **2016**, *352* (6282), 231-235.
- (13) Canto, C.; Houtkooper, R. H.; Pirinen, E.; Youn, D. Y.; Oosterveer, M. H.; Cen, Y.; Fernandez-Marcos, P. J.; Yamamoto, H.; Andreux, P. A.; Cettour-Rose, P.; Gademann, K.; Rinsch, C.; Schoonjans, K.; Sauve, A. A.; Auwerx, J. The NAD⁺ precursor nicotinamide riboside enhances oxidative metabolism and protects against high-fat diet-induced obesity. *Cell Metab.* **2012**, *15* (6), 838-847.
- (14) Cameron, A. M.; Castoldi, A.; Sanin, D. E.; Flachsmann, L. J.; Field, C. S.; Puleston, D. J.; Kyle, R. L.; Patterson, A. E.; Haessler, F.; Buescher, J. M.; Kelly, B.; Pearce, E. L.; Pearce, E. J. Inflammatory macrophage dependence on NAD(+) salvage is a consequence of reactive oxygen species-mediated DNA damage. *Nat. Immunol.* **2019**, *20* (4), 420-432.
- (15) Nacarelli, T.; Lau, L.; Fukumoto, T.; Zundell, J.; Fatkhutdinov, N.; Wu, S.; Aird, K. M.; Iwasaki, O.; Kossenkov, A. V.; Schultz, D.; Noma, K.-i.; Baur, J. A.; Schug, Z.; Tang, H.-Y.; Speicher, D. W.; David, G.; Zhang, R. NAD⁺ metabolism governs the proinflammatory senescence-associated secretome. *Nat. Cell Biol.* **2019**, *21* (3), 397-407.
- (16) Covarrubias, A. J.; Kale, A.; Perrone, R.; Lopez-Dominguez, J. A.; Pisco, A. O.; Kasler, H. G.; Schmidt, M. S.; Heckenbach, I.; Kwok, R.; Wiley, C. D.; Wong, H.-S.; Gibbs, E.; Iyer, S. S.; Basisty, N.; Wu, Q.; Kim, I.-J.; Silva, E.; Vitangcol, K.; Shin, K.-O.; Lee, Y.-M.; Riley, R.; Ben-Sahra, I.; Ott, M.; Schilling, B.; Scheibye-Knudsen, M.; Ishihara, K.; Quake, S. R.; Newman, J.; Brenner, C.; Campisi, J.; Verdin, E. Senescent cells promote tissue NAD⁺ decline during ageing via the activation of CD38(+) macrophages. *Nat. Metab.* **2020**, *2* (11), 1265-1283
- (17) Mehr, A. P.; Tran, M. T.; Ralto, K. M.; Leaf, D. E.; Washco, V.; Messmer, J.; Lerner, A.; Kher, A.; Kim, S. H.; Khoury, C. C.; Herzig, S. J.; Trovato, M. E.; Simon-Tillaux, N.; Lynch, M. R.; Thadhani, R. I.; Clish, C. B.; Khabbaz, K. R.; Rhee, E. P.; Waikar, S. S.; Berg, A. H.; Parikh, S. M. De novo NAD⁺ biosynthetic impairment in acute kidney injury in humans. *Nat. Med.* **2018**, *24* (9), 1351-1359.
- (18) Cardoso, D.; Muchir, A. Need for NAD⁺: Focus on striated muscle laminopathies. *Cells* **2020**, *9* (10), 2248.
- (19) Yoshino, J.; Baur, J. A.; Imai, S.-i. NAD⁺ intermediates: the biology and therapeutic potential of NMN and NR. *Cell Metab.* **2018**, *27* (3), 513-528.
- (20) Li, F.-L.; Shi, Y.; Zhang, J.-X.; Gao, J.; Zhang, Y.-W. Cloning, expression, characterization and homology modeling of a novel water-forming NADH oxidase from *Streptococcus mutans* ATCC 25175. *Int. J. Biol. Macromol.* **2018**, *113*, 1073-1079.
- (21) Gao, M.; Wang, Z.; Zheng, H.; Wang, L.; Xu, S.; Liu, X.; Li, W.; Pan, Y.; Wang, W.; Cai, X. Two-dimensional Tin selenide (SnSe) nanosheets capable of mimicking key dehydrogenases in cellular metabolism. *Angew. Chem. Int. Edit.* **2020**, *59* (9), 3618-3623.
- (22) Wu, D.; Li, J.; Xu, S.; Xie, Q.; Pan, Y.; Liu, X.; Ma, R.; Zheng, H.; Gao, M.; Wang, W. Engineering Fe-N doped graphene to mimic biological functions of NADPH oxidase in cells. *J. Am. Chem. Soc.* **2020**, *142* (46), 19602-19610.
- (23) Liu, W.; Zhang, L.; Liu, X.; Liu, X.; Yang, X.; Miao, S.; Wang, W.; Wang, A.; Zhang, T. Discriminating catalytically active FeN_x species of atomically dispersed Fe-N-C catalyst for selective oxidation of the C-H bond. *J. Am. Chem. Soc.* **2017**, *139* (31), 10790-10798.
- (24) Xie, J.; Kammert, J. D.; Kaylor, N.; Zheng, J. W.; Choi, E.; Pham, H. N.; Sang, X.; Stavitski, E.; Attenkofer, K.; Unocic, R. R.; Datye, A. K.; Davis, R. J. Atomically dispersed Co and Cu on N-doped carbon for reactions involving C-H activation. *ACS Catal.* **2018**, *8* (5), 3875-3884.
- (25) Deng, D.; Chen, X.; Yu, L.; Wu, X.; Liu, Q.; Liu, Y.; Yang, H.; Tian, H.; Hu, Y.; Du, P.; Si, R.; Wang, J.; Cui, X.; Li, H.; Xiao, J.; Xu, T.; Deng, J.; Yang, F.; Duchesne, P. N.; Zhang, P.; Zhou, J.; Sun, L.; Li, J.; Pan, X.; Bao, X. A single iron site confined in a graphene matrix for the catalytic oxidation of benzene at room temperature. *Sci. Adv.* **2015**, *1* (11), e1500462.

- (26) Parton, R. F.; Neys, P. E.; Jacobs, P. A.; Sosa, R. C.; Rouxhet, P. G. Iron-phthalocyanine immobilized on activated carbon black: A selective catalyst for alkane oxidation. *J. Catal.* **1996**, *164* (2), 341-346.
- (27) Pereira Monteiro, C. J.; Ferreira Faustino, M. A.; Pinho Morgado Silva Neves, M. d. G.; Quialheiro Simoes, M. M.; Sanjust, E. Metallophthalocyanines as catalysts in aerobic oxidation. *Catalysts* **2021**, *11* (1), 122.
- (28) Wang, D.; Jana, D.; Zhao, Y. Metal-organic framework derived nanozymes in biomedicine. *Accounts Chem. Res.* **2020**, *53* (7), 1389-1400.
- (29) Wu, J.; Wang, X.; Wang, Q.; Lou, Z.; Li, S.; Zhu, Y.; Qin, L.; Wei, H. Nanomaterials with enzyme-like characteristics (nanozymes): next-generation artificial enzymes (II). *Chem. Soc. Rev.* **2019**, *48* (4), 1004-1076.
- (30) Huang, L.; Chen, J.; Gan, L.; Wang, J.; Dong, S. Single-atom nanozymes. *Sci. Adv.* **2019**, *5* (5), eaav5490.
- (31) Jiao, L.; Kang, Y.; Chen, Y.; Wu, N.; Wu, Y.; Xu, W.; Wei, X.; Wang, H.; Gu, W.; Zheng, L.; Song, W.; Zhu, C. Unsymmetrically coordinated single Fe-N3S1 sites mimic the function of peroxidase. *Nano Today* **2021**, *40*, 101261.
- (32) Lu, M.; Wang, C.; Ding, Y.; Peng, M.; Zhang, W.; Li, K.; Wei, W.; Lin, Y. Fe-N/C single-atom catalysts exhibiting multienzyme activity and ROS scavenging ability in cells. *Chem. Commun.* **2019**, *55* (96), 14534-14537.
- (33) Ji, S.; Jiang, B.; Hao, H.; Chen, Y.; Dong, J.; Mao, Y.; Zhang, Z.; Gao, R.; Chen, W.; Zhang, R.; Liang, Q.; Li, H.; Liu, S.; Wang, Y.; Zhang, Q.; Gu, L.; Duan, D.; Liang, M.; Wang, D.; Yan, X.; Li, Y. Matching the kinetics of natural enzymes with a single-atom iron nanozyme. *Nat. Catal.* **2021**, *4* (5), 407-417.
- (34) Wang, Y.; Huang, R.; Han, J. W. Metal-nitrogen-carbon-based nanozymes: Advances and perspectives. *J. Phys. D Appl Phys.* **2022**, *55*, 323001.
- (35) Zhang, C.; Chen, C.; Zhao, D.; Kang, G.; Liu, F.; Yang, F.; Lu, Y.; Sun, J. Multienzyme cascades based on highly efficient metal-nitrogen-carbon nanozymes for construction of versatile bioassays. *Anal. Chem.* **2022**, *94* (8), 3485-3493.
- (36) Wang, Z.; Zhang, R.; Yan, X.; Fan, K. Structure and activity of nanozymes: Inspirations for de novo design of nanozymes. *Mater. Today* **2020**, *41*, 81-119.
- (37) Zitolo, A.; Goellner, V.; Armel, V.; Sougrati, M.-T.; Mineva, T.; Stievano, L.; Fonda, E.; Jaouen, F. Identification of catalytic sites for oxygen reduction in iron- and nitrogen-doped graphene materials. *Nat. Mater.* **2015**, *14* (9), 937-942.
- (38) Li, J.; Prslja, P.; Shinagawa, T.; Martin Fernandez, A. J.; Krumeich, F.; Artyushkova, K.; Atanassov, P.; Zitolo, A.; Zhou, Y.; Garcia-Muelas, R.; Lopez, N.; Perez-Ramirez, J.; Jaouen, F. Volcano trend in electrocatalytic CO₂ reduction activity over atomically dispersed metal sites on nitrogen-doped carbon. *ACS Catal.* **2019**, *9* (11), 10426-10439.
- (39) Tuinstra, F.; Koenig, J. L. Raman spectrum of graphite. *J. Chem. Phys.* **1970**, *53* (3), 1126-1130.
- (40) Sun, Y.; Silvioli, L.; Sahraie, N. R.; Ju, W.; Li, J.; Zitolo, A.; Li, S.; Bagger, A.; Arnarson, L.; Wang, X.; Moeller, T.; Bernsmeier, D.; Rossmeisl, J.; Jaouen, F.; Strasser, P. Activity-selectivity trends in the electrochemical production of hydrogen peroxide over single-site metal-nitrogen-carbon catalysts. *J. Am. Chem. Soc.* **2019**, *141* (31), 12372-12381.
- (41) Chung, H. T.; Cullen, D. A.; Higgins, D.; Sneed, B. T.; Holby, E. F.; More, K. L.; Zelenay, P. Direct atomic-level insight into the active sites of a high-performance PGM-free ORR catalyst. *Science* **2017**, *357* (6350), 479-483.
- (42) Li, J.; Jiao, L.; Wegener, E.; Richard, L. L.; Liu, E.; Zitolo, A.; Sougrati, M. T.; Mukerjee, S.; Zhao, Z.; Huang, Y.; Yang, F.; Zhong, S.; Xu, H.; Kropf, A. J.; Jaouen, F.; Myers, D. J.; Jia, Q. Evolution pathway from iron compounds to Fe-1(II)-N-4 sites through gas-phase iron during pyrolysis. *J. Am. Chem. Soc.* **2020**, *142* (3), 1417-1423.
- (43) Kang, J.; Sangwan, V. K.; Wood, J. D.; Hersam, M. C. Solution-based processing of monodisperse two-dimensional nanomaterials. *Acc. Chem. Res.* **2017**, *50* (4), 943-951.
- (44) Bae, G.; Kim, H.; Choi, H.; Jeong, P.; Kim, D. H.; Kwon, H. C.; Lee, K.-S.; Choi, M.; Oh, H.-S.; Jaouen, F.; Choi, C. H. Quantification of active site density and turnover frequency: From single-atom metal to nanoparticle electrocatalysts. *JACS Au* **2021**, *1* (5), 586-597.
- (45) Lyu, Y.; Scrimin, P. Mimicking enzymes: The quest for powerful catalysts from simple molecules to nanozymes. *ACS Catal.* **2021**, *11* (18), 11501-11509.
- (46) Lunov, O.; Syrovets, T.; Loos, C.; Beil, J.; Delecher, M.; Tron, K.; Nienhaus, G. U.; Musyanovych, A.; Mailaender, V.; Landfester, K.; Simmet, T. Differential uptake of functionalized polystyrene nanoparticles by human macrophages and a monocytic cell line. *ACS nano* **2011**, *5* (3), 1657-1669.
- (47) Buck, M. D.; O'Sullivan, D.; Geltink, R. I. K.; Curtis, J. D.; Chang, C.-H.; Sanin, D. E.; Qiu, J.; Kretz, O.; Braas, D.; van der Windt, G. J. W.; Chen, Q.; Huang, S. C.-C.; O'Neill, C. M.; Edelson, B. T.; Pearce, E. J.; Sesaki, H.; Huber, T. B.; Rambold, A. S.; Pearce, E. L. Mitochondrial dynamics controls T cell fate through metabolic programming. *Cell* **2016**, *166* (1), 63-76.
- (48) Vafai, S. B.; Mootha, V. K. Mitochondrial disorders as windows into an ancient organelle. *Nature* **2012**, *491* (7424), 374-383.
- (49) Mitchell, S. J.; Bernier, M.; Aon, M. A.; Cortassa, S.; Kim, E. Y.; Fang, E. F.; Palacios, H. H.; Ali, A.; Navas-Enamorado, I.; Di

- Francesco, A.; Kaiser, T. A.; Waltz, T. B.; Zhang, N.; Ellis, J. L.; Elliott, P. J.; Frederick, D. W.; Bohr, V. A.; Schmidt, M. S.; Brenner, C.; Sinclair, D. A.; Sauve, A. A.; Baur, J. A.; de Cabo, R. Nicotinamide improves aspects of healthspan, but not lifespan, in mice. *Cell Metab.* **2018**, *27* (3), 667-676.
- (50) Trammell, S. A. J.; Schmidt, M. S.; Weidemann, B. J.; Redpath, P.; Jaksch, F.; Dellinger, R. W.; Li, Z.; Abel, E. D.; Migaud, M. E.; Brenner, C. Nicotinamide riboside is uniquely and orally bioavailable in mice and humans. *Nat. Commun.* **2016**, *7* (1), 12948.
- (51) Brakedal, B.; Dolle, C.; Riemer, F.; Ma, Y.; Nido, G. S.; Skeie, G. O.; Craven, A. R.; Schwarzmuller, T.; Brekke, N.; Diab, J.; Sverkeli, L.; Skjeie, V.; Varhaug, K.; Tysnes, O.-B.; Peng, S.; Haugarvoll, K.; Ziegler, M.; Gruner, R.; Eidelberg, D.; Tzoulis, C. The NADPARK study: A randomized phase I trial of nicotinamide riboside supplementation in Parkinson's disease. *Cell Metab.* **2022**, *34* (3), 396-407.
- (52) Goodman, R. P.; Markhard, A. L.; Shah, H.; Sharma, R.; Skinner, O. S.; Clish, C. B.; Deik, A.; Patgiri, A.; Hsu, Y.-H. H.; Masia, R.; Noh, H. L.; Suk, S.; Goldberger, O.; Hirschhorn, J. N.; Yellen, G.; Kim, J. K.; Mootha, V. K. Hepatic NADH reductive stress underlies common variation in metabolic traits. *Nature* **2020**, *583* (7814), 122-126.
- (53) Patgiri, A.; Skinner, O. S.; Miyazaki, Y.; Schleifer, G.; Marutani, E.; Shah, H.; Sharma, R.; Goodman, R. P.; To, T.-L.; Bao, X. R.; Ichinose, F.; Zapol, W. M.; Mootha, V. K. An engineered enzyme that targets circulating lactate to alleviate intracellular NADH:NAD(+) imbalance. *Nat. Biotech.* **2020**, *38* (3), 309-313.
- (54) Orecchioni, M.; Ménard-Moyon, C.; Delogu, L. G.; Bianco, A. Graphene and the immune system: challenges and potentiality. *Adv. Drug Deliv. Rev.* **2016**, *105*, 163-175.
- (55) Heller, D. A.; Jena, P. V.; Pasquali, M.; Kostarelos, K.; Delogu, L. G.; Meidl, R. E.; Rotkin, S. V.; Scheinberg, D. A.; Schwartz, R. E.; Terrones, M. Banning carbon nanotubes would be scientifically unjustified and damaging to innovation. *Nat. Nanotech.* **2020**, *15* (3), 164-166.
- (56) Gazzì, A.; Fusco, L.; Orecchioni, M.; Ferrari, S.; Franzoni, G.; Yan, J. S.; Rieckher, M.; Peng, G.; Lucherelli, M. A.; Vacchi, I. A. Graphene, other carbon nanomaterials and the immune system: toward nanoimmunity-by-design. *J. Phys. Mater.* **2020**, *3* (3), 034009.
- (57) Guiney, L. M.; Wang, X.; Xia, T.; Nel, A. E.; Hersam, M. C. Assessing and mitigating the hazard potential of two-dimensional materials. *ACS nano* **2018**, *12* (7), 6360-6377.
- (58) Zheng, H.; Jiang, J.; Xu, S.; Liu, W.; Xie, Q.; Cai, X.; Zhang, J.; Liu, S.; Li, R. Nanoparticle-induced ferroptosis: detection methods, mechanisms and applications. *Nanoscale* **2021**, *13* (4), 2266-2285.
- (59) Jasim, D. A.; Menard-Moyon, C.; Begin, D.; Bianco, A.; Kostarelos, K. Tissue distribution and urinary excretion of intravenously administered chemically functionalized graphene oxide sheets. *Chem. Sci.* **2015**, *6* (7), 3952-3964.
- (60) Cao, J.; Yang, Q.; Jiang, J.; Dalu, T.; Kadushkin, A.; Singh, J.; Fakhrullin, R.; Wang, F.; Cai, X.; Li, R. Coronas of micro/nano plastics: a key determinant in their risk assessments. *Part. Fibre Toxicol.* **2022**, *19* (1), 55.
- (61) Ren, J.; Andrikopoulos, N.; Velonia, K.; Tang, H.; Cai, R.; Ding, F.; Ke, P. C.; Chen, C. Chemical and biophysical signatures of the protein corona in nanomedicine. *J. Am. Chem. Soc.* **2022**, *144* (21), 9184-9205
- (62) Cao, M.; Cai, R.; Zhao, L.; Guo, M.; Wang, L.; Wang, Y.; Zhang, L.; Wang, X.; Yao, H.; Xie, C. Molybdenum derived from nanomaterials incorporates into molybdenum enzymes and affects their activities in vivo. *Nat. Nanotech.* **2021**, *16* (6), 708-716.
- (63) Martin, C.; Jun, G.; Schurhammer, R.; Reina, G.; Chen, P.; Bianco, A.; Menard-Moyon, C. Enzymatic degradation of graphene quantum dots by human peroxidases. *Small* **2019**, *15* (52), 1905405.
- (64) Lalwani, G.; Xing, W.; Sitharaman, B. Enzymatic degradation of oxidized and reduced graphene nanoribbons by lignin peroxidase. *J. Mater. Chem. B* **2014**, *2* (37), 6354-6362.
- (65) Ryu, J.; Bregante, D. T.; Howland, W. C.; Bisbey, R. P.; Kaminsky, C. J.; Surendranath, Y. Thermochemical aerobic oxidation catalysis in water can be analysed as two coupled electrochemical half-reactions. *Nat. Catal.* **2021**, *4* (9), 742-752.
- (66) Rojas-Carbonell, S.; Artyushkova, K.; Serov, A.; Santoro, C.; Matanovic, I.; Atanassov, P. Effect of pH on the activity of platinum group metal-free catalysts in oxygen reduction reaction. *ACS Catal.* **2018**, *8* (4), 3041-3053.
- (67) Bates, J. S.; Biswas, S.; Suh, S.-E.; Johnson, M. R.; Mondal, B.; Root, T. W.; Stahl, S. S. Chemical and electrochemical O₂ reduction on earth-abundant MNC catalysts and implications for mediated electrolysis. *J. Am. Chem. Soc.* **2022**, *144* (2), 922-927.
- (68) Rojas-Carbonell, S.; Artyushkova, K.; Serov, A.; Santoro, C.; Matanovic, I.; Atanassov, P. Effect of pH on the activity of platinum group metal-free catalysts in oxygen reduction reaction. *ACS Catal.* **2018**, *8* (4), 3041-3053.
- (69) Jiao, L.; Li, J.; Richard, L. L.; Sun, Q.; Stracensky, T.; Liu, E.; Sougrati, M. T.; Zhao, Z.; Yang, F.; Zhong, S.; Xu, H.; Mukerjee, S.; Huang, Y.; Cullen, D. A.; Park, J. H.; Ferrandon, M.; Myers, D. J.; Jaouen, F.; Jia, Q. Chemical vapour deposition of Fe-N-C oxygen reduction catalysts with full utilization of dense Fe-N-4 sites. *Nat. Mater.* **2021**, *20* (10), 1385-1391.
- (70) Jia, Y.; Xiong, X.; Wang, D.; Duan, X.; Sun, K.; Li, Y.; Zheng, L.; Lin, W.; Done, M.; Zhang, G.; Liu, W.; Sun, X. Atomically dispersed Fe-N-4 modified with precisely located S for highly efficient oxygen reduction. *Nanomicro Lett.* **2020**, *12* (1), 116.
- (71) Armel, V.; Hannauer, J.; Jaouen, F. Effect of ZIF-8 crystal size on

the O₂ electro-reduction performance of pyrolyzed Fe-N-C catalysts. *Catalysts* **2015**, *5* (3), 1333-1351.

(72) Xu, X.; Xia, Z.; Zhang, X.; Li, H.; Wang, S.; Sun, G. Size-dependence of the electrochemical performance of Fe-N-C catalysts for the oxygen reduction reaction and cathodes of direct methanol fuel cells. *Nanoscale* **2020**, *12* (5), 3418-3423.

Table of Contents

